

Cite this: *Nanoscale Adv.*, 2021, 3, 6427

# Morphology-induced spectral modification of self-assembled WS<sub>2</sub> pyramids†

Irina Komen,  Sabrya E. van Heijst,  Sonia Conesa-Boj and L. Kuipers\*

Due to their intriguing optical properties, including stable and chiral excitons, two-dimensional transition metal dichalcogenides (2D-TMDs) hold the promise of applications in nanophotonics. Chemical vapor deposition (CVD) techniques offer a platform to fabricate and design nanostructures with diverse geometries. However, the more exotic the grown nanogeometry, the less is known about its optical response. WS<sub>2</sub> nanostructures with geometries ranging from monolayers to hollow pyramids have been created. The hollow pyramids exhibit a strongly reduced photoluminescence with respect to horizontally layered tungsten disulphide, facilitating the study of their clear Raman signal in more detail. Excited resonantly, the hollow pyramids exhibit a great number of higher-order phononic resonances. In contrast to monolayers, the spectral features of the optical response of the pyramids are position dependent. Differences in peak intensity, peak ratio and spectral peak positions reveal local variations in the atomic arrangement of the hollow pyramid crater and sides. The position-dependent optical response of hollow WS<sub>2</sub> pyramids is characterized and attributed to growth-induced nanogeometry. Thereby the first steps are taken towards producing tunable nanophotonic devices with applications ranging from opto-electronics to non-linear optics.

Received 1st July 2021  
Accepted 21st September 2021

DOI: 10.1039/d1na00531f

rsc.li/nanoscale-advances

## 1. Introduction

Two-dimensional transition metal dichalcogenites (2D-TMDs) have recently attracted enormous scientific attention for their distinctive optical properties. Like graphene, TMD materials consist of layers held together only by van der Waals forces. 2D TMDs (*e.g.* MoS<sub>2</sub>, WS<sub>2</sub>, MoSe<sub>2</sub>, WSe<sub>2</sub> *etc.*) are atomically thin semiconductors, with a transition from indirect to direct bandgap in the few-layer limit.<sup>1</sup> Due to their high binding energy, electron–hole pairs form stable excitons even at room-temperature. A pseudospin can be attributed to each of the two valleys 2D TMDs possess, making it possible to address them selectively with circularly polarized light.<sup>2–4</sup> The electronic and optical properties of these 2D semiconductors, for instance the excitons and valley pseudospin, make them an interesting platform for opto-electronics<sup>5,6</sup> and valleytronics<sup>7–9</sup> applications.

One of the ways of creating 2D TMD monolayer samples is by exfoliation from bulk.<sup>9</sup> An alternative method to produce layered TMDs materials is Chemical Vapor Deposition

(CVD).<sup>10–15</sup> While CVD can reproduce horizontal layers as found in naturally occurring TMDs, adjusting the growth conditions enables the growth of nanostructures with exciting properties and applications in nanotechnology, for instance vertical walls, flowers and pyramids.<sup>16</sup> Under certain CVD growth parameters TMDs materials form pyramid-like structures,<sup>17,18</sup> having many active adsorption sites useful for applications in hydrogen sensors<sup>19</sup> and water disinfection,<sup>20</sup> at the same time possessing interesting electronic properties like ferromagnetism<sup>21</sup> and high mobility.<sup>22,23</sup> Moreover, pyramid-like TMDs structures have applications in non-linear optics,<sup>22,24,25</sup> as they exhibit higher non-linear optical conversion efficiency than monolayers due to the thickness increase, while demonstrating a much larger non-linear optical response than multilayer TMDs.

It is interesting to note that only in a limited number of studies in the literature photoluminescence of these spiral- or pyramid-like structures is reported.<sup>17,18,20,22</sup> In some, the non linear optical response is studied.<sup>22,24,25</sup> In most, the TMDs spirals and pyramids are studied using Raman spectroscopy.<sup>17–24</sup> However, comparing the measured optical response of pyramid-like structures of different studies needs to be done with caution, as the terms spiral flake or pyramid are used for nanostructures that have different thicknesses, geometry and sizes.

Raman spectroscopy is a powerful tool to study 2D TMDs, as knowledge on the vibrational modes of the layers provides insights in their structure.<sup>26–28</sup> Commonly studied are the characteristic vibrational modes of TMDs, the E<sub>2g</sub><sup>1</sup> that

*Kavli Institute of Nanoscience, Department of Quantum Nanoscience, Delft University of Technology, The Netherlands. E-mail: L.Kuipers@tudelft.nl*

† Electronic supplementary information (ESI) available: SEM and ADF-STEM images for more information about the morphology and crystal structure of the hollow pyramids. Discussion about the origin of the background in the spectral response of the pyramids. Comparison of the spectral features (Raman intensity, peak ratio and peak position) of the hollow WS<sub>2</sub> pyramid at different temperatures, and between the WS<sub>2</sub> monolayer, hollow pyramid and full pyramid. Overview of the measured Raman features. See DOI: 10.1039/d1na00531f



corresponds to the in-plane displacement of the atoms, and the  $A_{1g}$  that corresponds to the out-of-plane displacement of the chalcogenide atoms, as well as the longitudinal acoustic phonon LA(M).<sup>27–30</sup> Studying the Raman response as a function of temperature,<sup>31–35</sup> excitation polarization<sup>27,29,36</sup> and excitation wavelength,<sup>37–39</sup> provides information on structural properties like number of layers, strain and defect density.

It is important to note that the existence of exciton resonances in 2D TMDs has large implications for its Raman response. Raman features are greatly enhanced when the excitation is in resonance with an excitonic transition.<sup>27,28,37–40</sup> Resonance Raman spectroscopy on 2D TMDs materials results in the excitation of higher-order phononic resonances,<sup>41</sup> which yields rich Raman spectra with many more modes than the two mentioned characteristic modes.

Many questions arise about the nature of the optical response from complex CVD-grown TMDs pyramid-like nanostructures. It is unknown how the nanogeometry of TMDs pyramids influences its photoluminescence and Raman response and how it depends on temperature and polarization. For potential applications, this knowledge is paramount.

Here, we study the Raman and photoluminescence response of CVD-grown hollow WS<sub>2</sub> pyramids, comparing it to the optical response of WS<sub>2</sub> monolayers. Even though the WS<sub>2</sub> monolayers and pyramids are grown on the same substrate and under the same conditions, their measured optical response is completely different. We find, surprisingly, that the pyramids exhibit a strongly reduced photoluminescence (PL) with respect to horizontal layers. The reduced PL enables us to study the Raman signal of the hollow WS<sub>2</sub> pyramids, that contains both the characteristic Raman peaks of flat layers and a great number of higher-order phononic resonances. In contrast with the monolayers, the measured optical response of the hollow WS<sub>2</sub> pyramids is non-uniform over the nanostructures. Annular dark-field (ADF) scanning transmission electron microscopy (STEM) measurements confirm position-dependent variations in atomic arrangement.

## II. Results and discussion

### A. Hollow WS<sub>2</sub> pyramids

Fig. 1a presents an SEM image of a CVD-grown hollow WS<sub>2</sub> pyramid (the substrate is a SiN film on Si, see Methods). The WS<sub>2</sub> is crystallized in a 3R-phase (see Fig. S2c, d and Section 1 in the ESI†). The clear lines along the pyramid sides indicate single steps (see Fig. S1c and S2a, b in the ESI†). The geometry of the darker middle becomes more clear when examining the AFM image in Fig. 1b. The height profile measured with the AFM along the blue line is presented in Fig. 1c. The bottom of the crater in the middle is roughly 5.6 nm high with respect to the substrate, whereas the pyramid sides reach a height of 44 nm. The inset of Fig. 1a displays a schematic representation of the hollow pyramid, depicting the stair-like sides in white and the crater with a bottom of finite thickness in the middle.

Fig. 1e presents optical spectra obtained by exciting a WS<sub>2</sub> pyramid at the stair-like side with either a 595 nm laser (orange) or a 561 nm laser (green). The spectra contain a similar

sequence of peaks, but their spectral position does not overlap in wavelength. However, these peaks are located at the same relative frequency distance to the excitation laser, as depicted in Fig. 1f. The clear overlap of the larger peak positions in the spectra from the two different lasers indicates that the collected light originates from an inelastic Raman process rather than from photoluminescence.

Fig. 1d presents an SEM image of a single horizontal layer (monolayer) WS<sub>2</sub> grown on the same substrate (next to hollow pyramids and monolayers, also fully grown pyramids are present on this substrate, see ESI, Fig. S1a, S5 and S6†). Comparing in Fig. 1e the optical response of the monolayer (black dotted line) with that of the pyramid, it becomes apparent that the pyramid exhibits a strongly reduced photoluminescence with respect to monolayer WS<sub>2</sub>. A small background under the Raman modes is visible in the spectrum of the pyramid around the PL wavelength of 630 nm. If this is remnant PL emerging from the hollow WS<sub>2</sub> pyramid, it has an intensity of at most 1% of the WS<sub>2</sub> monolayer (see ESI Fig. S3†). The immense reduction of the photoluminescence intensity from the hollow pyramids is unexpected. Even though the pyramid crater is only a few nanometers thin, the pyramid spectra do not resemble spectra of standard few-layered horizontal WS<sub>2</sub> (see ESI Fig. S3†). When the WS<sub>2</sub> thickness increases from monolayer to bulk, it transitions from a direct to an indirect bandgap semiconductor.<sup>1</sup> It is important to note that, in contrast to the hollow pyramids, the reduced PL from the direct bandgap can be easily measured for few-layered WS<sub>2</sub>.<sup>1,9</sup> Moreover, the hollow WS<sub>2</sub> pyramids do not exhibit any luminescence at the known wavelength of the indirect bandgap, as would have been expected from both bulk and few-layer WS<sub>2</sub> (see ESI Fig. S3†). Therefore we conclude that the increase of the layer number from monolayer WS<sub>2</sub> to the pyramid crater cannot explain the reduction of the PL intensity. CVD-grown horizontal 2D TMDs flakes exhibit a similar amount of photoluminescence as exfoliated samples. Hence, the PL intensity reduction by at least two orders of magnitude of the hollow pyramids cannot merely be explained as being intrinsic to the CVD growth process, *e.g.* through an increase in defect density. Furthermore, the 3R-WS<sub>2</sub> nanostructure cannot explain the PL intensity reductions, as 3R-WS<sub>2</sub> exhibits the same photoluminescence as the naturally occurring 2H-WS<sub>2</sub>.<sup>42,43</sup>

We conclude that our hollow WS<sub>2</sub> pyramids have a lower quantum efficiency than WS<sub>2</sub> flakes: assuming that the optical absorption of a WS<sub>2</sub> monolayer and a pyramid is the same, the quantum efficiency of these pyramids is at least two orders of magnitude lower than that of a monolayer WS<sub>2</sub>. Given the fact that the pyramids have a thickness of 5–44 nm, it is safe to assume that a pyramid actually absorbs more than a monolayer, therefore the quantum efficiency is likely to be at least another order of magnitude lower. We attribute the decrease in the quantum efficiency to the increase in possible non-radiative loss channels due to the presence of all the edges in the structure of these pyramids. The increase in non-radiative loss channels due to the edges in the pyramid structure is therefore the main factor that leads to a severe quenching of the exciton photoluminescence, without influencing the Raman modes.



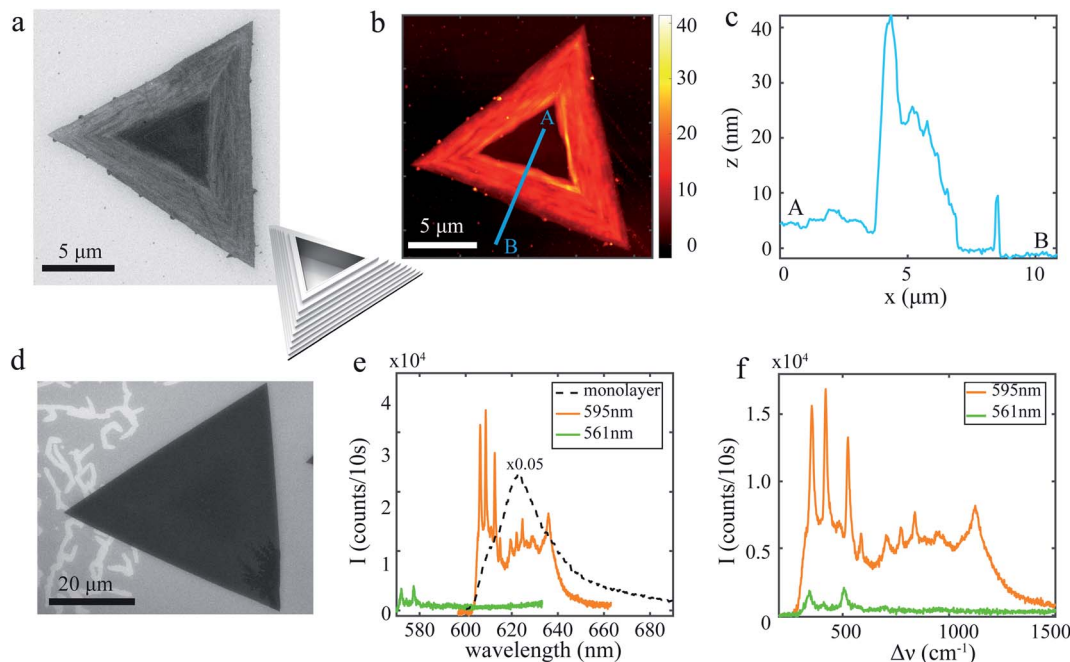


**Fig. 1** Hollow  $\text{WS}_2$  pyramids. (a) SEM image of the hollow  $\text{WS}_2$  pyramid. The lines along the sides indicate the single stair steps, whereas the darker region in the middle is the crater. (Inset) Schematic representation of the hollow pyramid. (b) AFM image of the hollow  $\text{WS}_2$  pyramid. The blue line indicates the position of the AFM crosscut depicted in (c), ranging from A the pyramid crater to B the substrate. (d) SEM image of a  $\text{WS}_2$  monolayer on the same substrate. (e) Photoluminescence spectrum of the  $\text{WS}_2$  monolayer (black dotted line), and spectra of a pyramid obtained with a 595 nm excitation (orange) and a 561 nm excitation (green). When converting the x-axis to wavenumber  $\Delta\nu$  in (f), the spectral response on the two different lasers overlaps nicely, indicating that the collected light originates from Raman processes rather than photoluminescence.

The reduction of the PL enables us to study the Raman response of the hollow  $\text{WS}_2$  pyramids in more detail, as many Raman features are usually obscured by the PL spectrum. The pyramid spectra obtained with the 595 nm excitation exhibit roughly 10–12 Raman features, three of which have not been reported before for neither horizontal  $\text{WS}_2$  layers nor  $\text{WS}_2$  nanostructures (see Fig. 3). For the 561 nm excitation, fewer Raman features are visible in the spectra, and these features have a lower intensity. This can be attributed to the fact that the 595 nm excitation light is close to the A-exciton resonance, whereas the 561 nm is out-of-resonance with both the A- and B-excitons. Raman modes of TMDs can be greatly enhanced when they are excited in resonance with an excitonic transition.<sup>27,28,38–40</sup>

## B. Structural characterization

In order to help interpret the studied optical response, we perform a detailed structural characterization of the hollow  $\text{WS}_2$  pyramids by means of Transmission Electron Microscopy measurements. Fig. 2 displays annular dark-field (ADF) scanning transmission electron microscopy (STEM) images taken in different regions of these  $\text{WS}_2$  nanostructures. Fig. 2a and b display atomic resolution ADF-STEM images of two different locations corresponding to the middle region of the hollow pyramid, while Fig. 2c corresponds to the pyramid side. By comparing these three images, we can clearly observe differences in the atomic arrangement. In Fig. 2a, the atomic distribution displays a well defined hexagonal shape, and this

symmetry is highlighted by the corresponding fast Fourier transform (see inset in Fig. 2a). As we can observe from Fig. 2b, the atomic arrangements at this location are somewhat different from those observed in Fig. 2a. This structural variation is also reflected in the corresponding FFT (inset in Fig. 2b), where one of the Bragg reflections exhibits a reduced intensity (marked with a yellow circle to facilitate its visualization). Structural variation is also observed in the side region of the hollow pyramid. The difference in contrast in Fig. 2c corresponds to two stair-like steps in the pyramid side. By comparing their relative atomic arrangement, we can determine that, while the external step exhibits a clear hexagonal honeycomb structure, this arrangement is lost in the subsequent layer. Note also that, as observed from the results obtained in the middle region of the nanostructures, even across its sides the atomic arrangement can vary slightly (see also Fig. S7† in the ESI†).

These subtle variations of the atomic arrangement might be induced by the local presence of strain, which in turn results into a slight change of the orientation of the flake. Importantly, the level of structural disorder is more marked in the middle of the pyramids as compared to the sides (see ESI Fig. S7†) due to the additional presence of free-standing  $\text{WS}_2$  flakes arising from the walls of the hollow pyramid.

## C. Characterization of vibrational modes

In Fig. 3a we present a  $\text{WS}_2$  pyramid spectrum, acquired at the pyramid side, in which all Raman features are indicated with arrows. Commonly, only three Raman modes are measured on





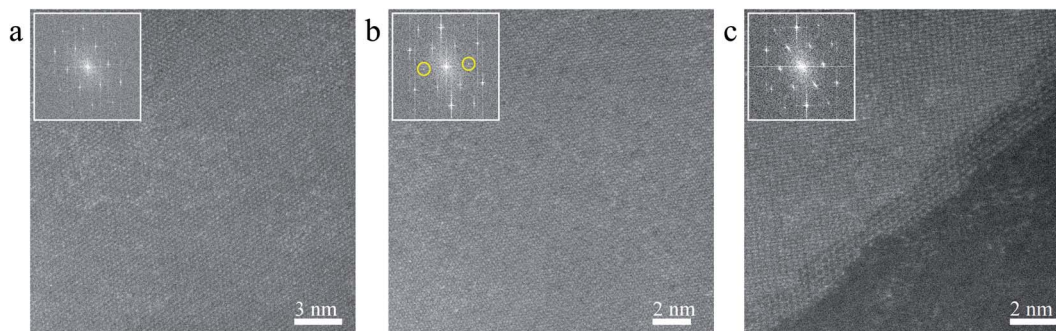


Fig. 2 ADF-STEM of a hollow  $\text{WS}_2$  pyramid atomic resolution. Annular dark-field scanning transmission electron microscopy images taken in (a and b) the middle region, and (c). The side of a hollow  $\text{WS}_2$  pyramid. Subtle variations in the atomic arrangement can be observed. The corresponding FFTs, as given as insets in each of the panels, highlight this feature further. Changes in the Bragg reflections occur between them. One of which is a reduction of the intensity of one of the Bragg reflections in the middle region of the hollow pyramid, as marked by the yellow circles in (b).

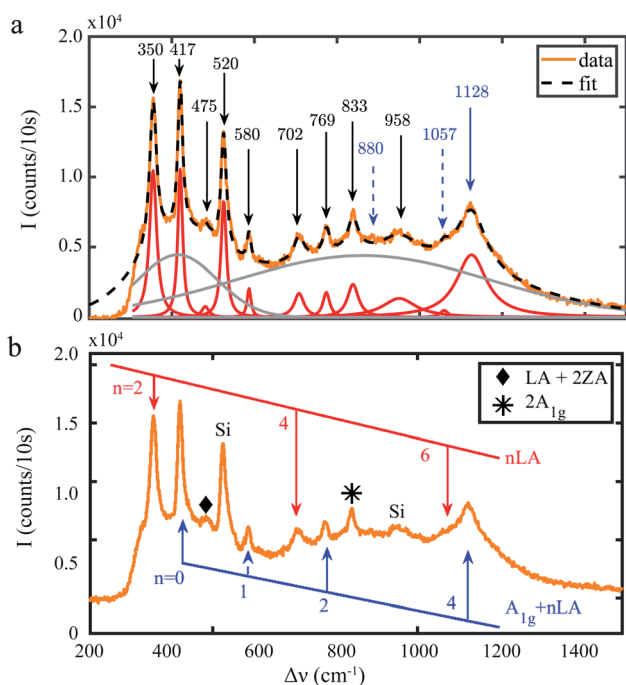


Fig. 3 Characterization of Raman peaks. (a) The optical response of the hollow pyramids (orange) can be fitted by eleven Lorentzian lineshapes (red) and two Gaussians (grey). The Raman features are indicated by arrows with their spectral position in  $\text{cm}^{-1}$ . The last three features (in blue) have not been reported before. (b) Part of the features can be explained as being multiphonon resonances involving the LA(M) phonon. The blue line depicts the higher order resonances of  $A_{1g} + n^*LA(M)$ . The red line depicts the higher order resonances of  $n^*LA(M)$ .

both horizontal TMDs layers or nanostructures. We measure 10–12 Raman features, three of which have not been reported previously (indicated in blue in Fig. 3a). The other modes can be attributed following a limited amount of previous investigations (see also Table 1). In order to analyze the spectra in more detail, we fit the overall spectrum with a collection of eleven Lorentzian lineshapes (red) and a background consisting of two

Gaussians (grey) (see ESI† Section 1 for a discussion on the background). This way we are able to attribute the new Raman modes from hollow  $\text{WS}_2$  pyramids to being multiphonon resonances involving the LA(M) phonon, adopting the methodology for high frequency Raman features in  $\text{MoS}_2$ .<sup>41</sup> The blue line in Fig. 3b depicts the higher order resonances of  $A_{1g} + n^*LA(M)$ . The peak  $580 \text{ cm}^{-1}$  is commonly attributed to  $A_{1g} + LA(M)$ ,<sup>28,30–32</sup> and the peak at  $769 \text{ cm}^{-1}$  is attributed to  $A_{1g} + 2LA(M)$  by Molas *et al.*<sup>30</sup> Thus we attribute the newly observed peak at  $1128 \text{ cm}^{-1}$  ( $n = 4$ ) to  $A_{1g} + 4LA(M)$ . The red line in Fig. 3b depicts the higher order resonances of  $n^*LA(M)$ . The peak at  $702 \text{ cm}^{-1}$  is commonly attributed to  $4LA(M)$ ,<sup>28,31</sup> which is twice the first  $2LA(M)$  Raman peak at  $350 \text{ cm}^{-1}$ . Therefore we attribute the newly observed small shoulder of the last peak around  $1057 \text{ cm}^{-1}$  to  $6LA(M)$ . The expected resonance at  $3LA(M)$  (red line in Fig. 3b) would spectrally overlap with the first silicon peak at  $520 \text{ cm}^{-1}$ , as well as the expected resonance at  $n = 3$  (blue line in Fig. 3b) would overlap with the second silicon peak  $955 \text{ cm}^{-1}$ , so these possible features cannot be distinguished from the substrate response. The expected  $5LA(M)$  (red line in Fig. 3b) would be around  $880 \text{ cm}^{-1}$ , but is too dim to distinguish very clearly from the background. The peak at  $833 \text{ cm}^{-1}$  is  $2^*A_{1g}$ , and the peak at  $475 \text{ cm}^{-1}$  is commonly attributed to  $LA(M) + 2ZA(M)$  (see Table 1). We conclude that the observed high-frequency Raman modes are multiphonon resonances involving the LA(M) phonon, excited because the  $595 \text{ nm}$  laser is in resonance with the A-exciton.

The highest frequency Raman modes have not been reported before on horizontal  $\text{WS}_2$  layers (indicated in blue in Fig. 3a). A possible explanation for not observing them on monolayers is that investigating Raman modes on horizontal  $\text{WS}_2$  layers is experimentally challenging because of the presence of photoluminescence, that is much brighter than any Raman feature. An intriguing alternative hypothesis is that the nanogeometry of the hollow pyramid plays a role in exciting the higher order Raman modes more resonantly, *e.g.* through a higher phonon density of states.



**Table 1** Overview of the measured Raman features on the hollow pyramid (see Fig. 3) at room-temperature. The first column gives the peak position determined by fitting, with the statistical standard deviation in the second column and the brightness in the third. The fourth column indicates known Raman modes, where the last column gives a few references. The fifth column indicates possible explanations, either taken from only one article or being our hypothesis

Position	Std (cm <sup>-1</sup> )	Brightness	Attributed to	Possibly	Literature
350 cm <sup>-1</sup>	1.6	++	E <sub>2g</sub> <sup>1</sup> /2LA(M)		27–31, 38 and 44
417 cm <sup>-1</sup>	1.5	++	A <sub>1g</sub>		27, 28, 30, 31, 38 and 44
475 cm <sup>-1</sup>	4.7	--	LA + 2ZA or E''(M) + TA(M)		30 and 39
520 cm <sup>-1</sup>	0.8	++	Si	3LA(M)	45–47
580 cm <sup>-1</sup>	1.0	+–	A <sub>1g</sub> + LA(M)		28, 30–32,44
702 cm <sup>-1</sup>	1.4	+	4LA(M)	2E <sub>2g</sub> <sup>1</sup>	28,31,44, (30)
769 cm <sup>-1</sup>	1.0	+	A <sub>1g</sub> + E <sub>2g</sub> <sup>1</sup>	A <sub>1g</sub> + 2LA(M)	30
833 cm <sup>-1</sup>	1.2	+	2A <sub>1g</sub>		30
880 cm <sup>-1</sup>		--		5LA(M)	
958 cm <sup>-1</sup>	3.3	+–	Si	A <sub>1g</sub> + 3LA(M)	45–47
1057 cm <sup>-1</sup>	1.0	--		6LA(M)	
1128 cm <sup>-1</sup>	4.0	+		A <sub>1g</sub> + 4LA(M)	

#### D. Position dependence of spectral features

The hollow WS<sub>2</sub> pyramids contain two distinct regions: the crater in the middle and the stair-like sides. We find that these regions exhibit a different spectral response. This is in contrast from the more homogeneous spectral response for horizontal WS<sub>2</sub> flakes (see ESI, Fig. S5 and S6†). Fig. 4a presents an intensity map of the first Raman peak (E<sub>2g</sub>, 2LA). To create this map, the maximum value of the fitted peak is used (see Fig. 3a).

The peak intensity is higher and the peaks are more pronounced at the pyramid crater than at the stair-like sides. For the other WS<sub>2</sub> Raman peaks, as well as at different temperatures and using different excitation wavelengths, this intensity distribution looks similar (see ESI Fig. S4†).

Fig. 4b presents an intensity map for the silicon peak at 520 cm<sup>-1</sup>. As expected, there is a constant intensity for the substrate next to the pyramid. It is interesting to note that the

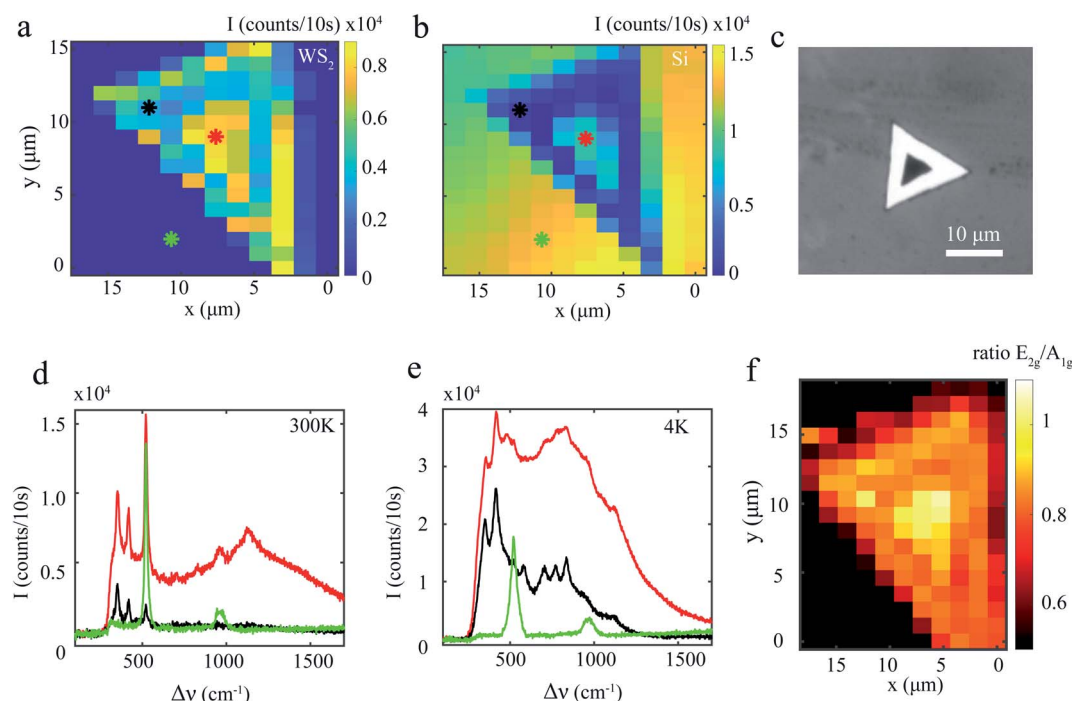


**Fig. 4** Position dependence of intensity and shape of spectra. (a) Intensity map of the first WS<sub>2</sub> Raman feature around 350 cm<sup>-1</sup>, with a step size of around 1.5 μm. The stars indicate the positions of the spectra in (d) and (e). Note that the x and y axis in the map are slightly skewed due to experimental constraints (see Experimental section). (b) Intensity map of the Si Raman peak at 520 cm<sup>-1</sup>. (c) Optical image of a hollow WS<sub>2</sub> pyramid. Note the white colour at the sides, indicating a clear increase in scattering from the sides with respect to the top. (d and e). Pyramid spectra at 300 K and 4 K. The substrate spectrum (green) shows the two Si peaks at 520 and 955 cm<sup>-1</sup>. The spectrum at the hollow part of the pyramid (red) has an overall higher intensity than at the side (black). (f). Map of the ratio between the first two Raman features in the spectra (E<sub>2g</sub>/A<sub>1g</sub>).



intensity of this substrate peak also decreases on the pyramid edges. We hypothesise that light scatters a lot from the stair-like pyramid sides, as seen from the bright white colour of the sides in the optical image (Fig. 4c). This both reduces the available excitation light to excite Raman modes, and scattering of the resulting Raman response reduces the detected light, including the Raman response of the silicon substrate. Fig. 4d and e depict spectra on three different positions: on the hollow pyramid middle (red), on the substrate (green) and on the pyramid side (black) (indicated by stars in Fig. 4a and b). In both the room temperature spectra in Fig. 4d and 4 K spectra in Fig. 4e (temperature dependence will be discussed later), the two silicon peaks at 520 and 955  $\text{cm}^{-1}$  can be clearly distinguished (in green). The spectrum at the pyramid crater (red) has clearly a higher overall intensity. In addition to the Raman peaks, there is also a background visible. Especially at 4 K, this background signal becomes extremely high, turning the signal from all the higher frequency Raman modes into mere shoulders. Based on its spectral position, we attribute this background to intermediate gap states or defect states (see ESI Fig. S3†). It is interesting to note that this background is significantly higher in the pyramid crater than on the sides, which might be originated by the presence of crystallographic defects.

Fig. 4f presents a map of the intensity ratio between the first two Raman peaks ( $E_{2g}/A_{1g}$ ). Just like the intensity of the individual peaks, this intensity ratio is also non-uniform over the  $\text{WS}_2$  pyramid. In the pyramid crater, the peak ratio is approximately 1.0, whereas on the stair-like sides, the  $A_{1g}$  peak is higher. The difference in peak ratio between the pyramid crater and sides is also present and much higher for the 561 nm excitation (see ESI Fig. S5†). Note that the spectral features of a fully grown pyramid are very similar to the spectral response from the hollow pyramid sides (see ESI Fig. S5†). We conclude that both the peak intensity and the overall shape of the spectra

are non-uniform along the  $\text{WS}_2$  pyramid, behaving differently at the hollow pyramid crater and the stair-like sides. This indicates a difference in the atomic arrangement between the two parts of the pyramid.

We also find a spatial non-uniformity in the spectral position of the peaks. Fig. 5a depicts the spectral position of the first  $\text{WS}_2$  Raman peak ( $E_{2g}$ , 2LA) as a function of position. This spectral position is fairly uniform over most of the nanostructure, except for the right edge, where the spectral position is red shifted significantly up to 320  $\text{cm}^{-1}$ . Moreover, a small blue shift of the peak is seen on the left pyramid edge. The second  $\text{WS}_2$  Raman peak exhibits a similar spectral shift (not shown), as do spectra obtained for a 561 nm excitation. This spectral shift of peaks becomes more evident when comparing the spectra at the positions of the blue stars (Fig. 5b). The second line indicates the position of the silicon peak at 520  $\text{cm}^{-1}$ , which is clearly constant in all three spectra. However, when comparing the line at 355  $\text{cm}^{-1}$  with the position of the first Raman peak, it is clear that the  $\text{WS}_2$  peaks in the spectrum are blue shifted.

The spectral position of Raman modes in TMD materials is known to depend on the number of layers.<sup>21,22,26–28</sup> One might therefore have expected a gradual spectral shift along the stair-like sides of the pyramid, because of their gradual increase in  $\text{WS}_2$  layer thickness. Unfortunately, the diffraction-limited laser spot of size 450 nm (see Methods) is much bigger than the width of the individual terraces. Therefore, if the size of the steps is one or even a few layers, we do not have the resolution to distinguish thickness-dependent changes in the Raman response of individual steps. The changes in the Raman response are smallest for low  $N$ , where  $N$  is the number of layers. The reported difference in spectral position for different layer thicknesses is at most 5  $\text{cm}^{-1}$  (between a monolayer and a bilayer), much less than the shift of 30  $\text{cm}^{-1}$  that we observe at the edge of this pyramid. Therefore this spectral shift cannot be explained by a thickness increase alone.

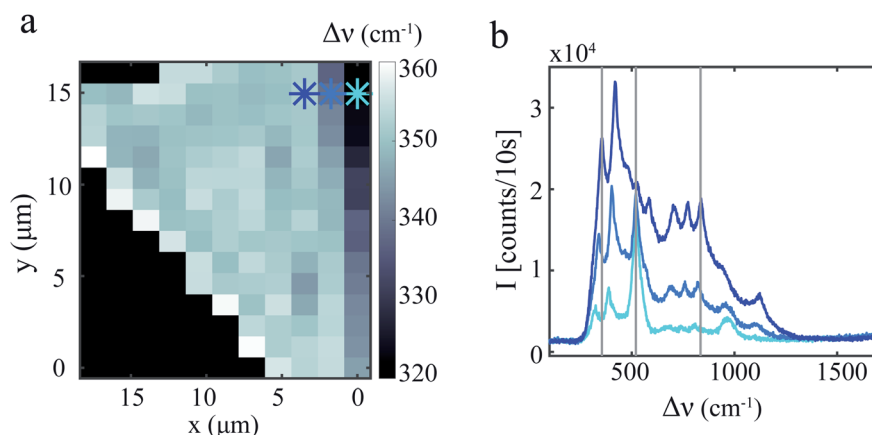


Fig. 5 Position dependence of spectral position. (a) Map at 4 K of the spectral position of the first  $\text{WS}_2$  Raman feature (2LA(M),  $E_{2g}$ ), with a step size of around 1.5  $\mu\text{m}$ . The spectral position is fairly homogeneous over most of the pyramid, except for the edge, where it is blue shifted up to 320  $\text{cm}^{-1}$ . The stars indicate the position of the spectra in (b). Three gray lines are drawn as guides to the eye. Comparing the position of the Si peak of the three spectra with the line at 520  $\text{cm}^{-1}$  indicates that the spectral position of this peak does not shift. Comparing the position of the first  $\text{WS}_2$  peak with the line at 355  $\text{cm}^{-1}$  does indicate the large shift of the spectrum on the pyramid edge (light blue) with respect to the rest of the nanostructure.



The spectral position of Raman modes in TMD materials does not only depend on the number of layers, it is also known to be influenced by the defect density,<sup>48,49</sup> strain<sup>50,51</sup> and pressure.<sup>33</sup> The reported shift due to strain is 2–3  $\text{cm}^{-1}$ <sup>50,51</sup> and due to an increased defect density is 5–10  $\text{cm}^{-1}$ .<sup>48,49</sup> For both strain and defects, the  $A_{1g}$  peak is much less affected than the  $E_{2g}$  peak. The reported shift due to pressure is up to 40  $\text{cm}^{-1}$  for pressures up to 20 GPa.<sup>33</sup> Since our measurements were performed in either ambient (room temperature) or vacuum (low temperature) conditions, we do not expect a spectral shift due to pressure. It is not unlikely that a large defect density and/or the presence of strain are present in the hollow pyramids. Interestingly, spectra taken on fully grown  $\text{WS}_2$  pyramids with curved edges do exhibit small shifts in the spectral peak position along the edges with highest curvature, where a higher stress or strain is expected (see ESI Fig. S6†). Therefore we assume that the origin of the large spectral shift in the hollow  $\text{WS}_2$  pyramid in Fig. 5 lies in a combination of the mentioned effects of defect density and strain or stress. Having said that, the previously reported shifts, even when added, are much lower than the 30  $\text{cm}^{-1}$  that we observe on the edge of the hollow pyramid, so

we cannot exclude unknown other causes related to the specific nanogeometry of the hollow pyramid.

In this context, it is interesting to note that we measure an average spectral position of the first Raman peak on a  $\text{WS}_2$  monolayer of 357  $\text{cm}^{-1}$ , which is higher than the average of 350  $\text{cm}^{-1}$  of this and other  $\text{WS}_2$  pyramids (see ESI Fig. S6†). Given that the first  $\text{WS}_2$  Raman feature is a combination of the  $E_{2g}$  and  $2\text{LA(M)}$  phonon, we hypothesise that the first Raman feature in the monolayer has a larger contribution from the  $E_{2g}$  than the same first feature in the hollow pyramid spectra.

We conclude that the spectral features of the hollow pyramids, namely intensity, peak ratio and spectral peak position, vary in space over the nanostructures. This in contrast with the homogeneous distributions of these spectral features on a  $\text{WS}_2$  monolayer. Moreover, the spectral position of the first  $\text{WS}_2$  Raman feature is different for a  $\text{WS}_2$  monolayer than for a hollow  $\text{WS}_2$  pyramid, indicating a larger contribution from the  $E_{2g}$  than the  $2\text{LA(M)}$  phonon.

### E. Temperature dependence of spectral features

Studying the temperature dependence of spectral features provides insights on the structural properties of the  $\text{WS}_2$

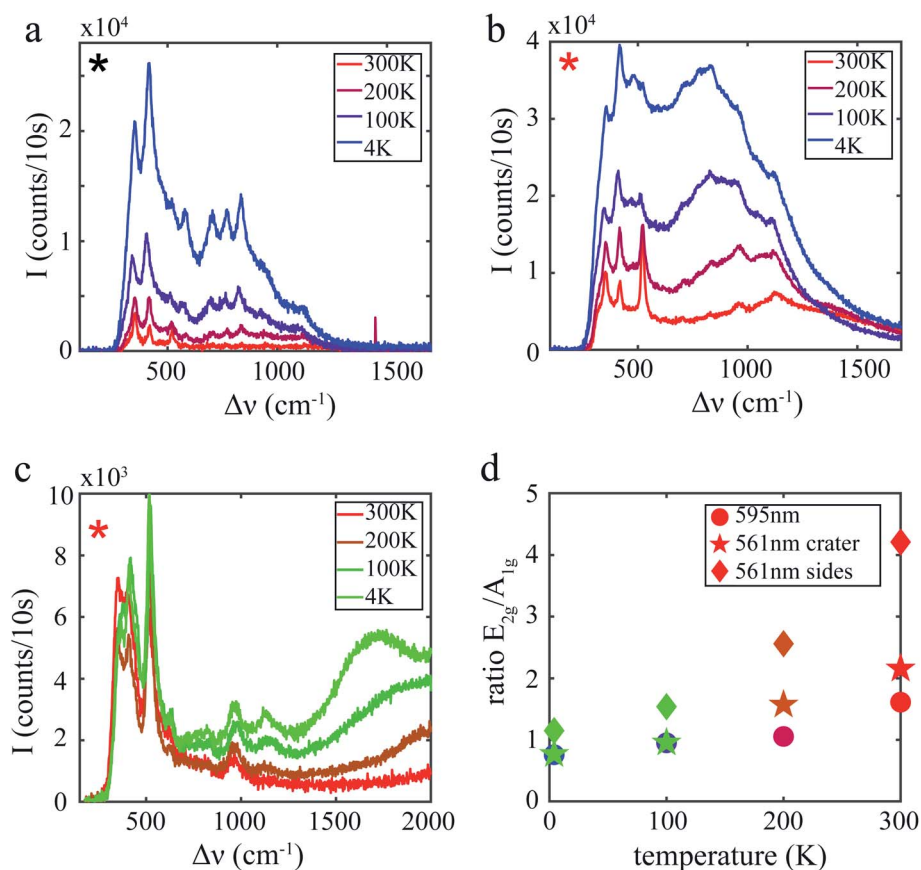


**Fig. 6** Temperature dependence of spectral features. (a and b) Spectra obtained as a function of temperature with a 595 nm excitation on the stair-like pyramid sides (black star in Fig. 4) and on the hollow pyramid middle (red star in Fig. 4), respectively. (c) Spectra obtained with a 561 nm excitation of the hollow pyramid middle as a function of temperature. The background visible at higher frequencies overlaps in wavelength with the background under the 595 nm spectra in Fig. 4b (see ESI Fig. S3†). (d) Temperature dependence of the intensity ratio of the first two Raman features, the fingerprint of  $\text{WS}_2$  material. The intensity ratio is presented for spectra upon 595 nm excitation (circles), spectra at the pyramid crater (stars) and pyramid sides (diamonds) upon 561 nm excitation.





pyramids. Fig. 6a presents spectra at four temperatures at the pyramid side (black star in Fig. 4a), obtained with a 595 nm excitation. With decreasing temperature, the Raman modes become more pronounced. Note for instance the three features at 702, 769 and 833  $\text{cm}^{-1}$ . The intensity of both the Raman features and the background increases with decreasing temperature. This intensity increase of the background is even more clear in Fig. 6b and c, that present the spectra from the hollow pyramid middle (red star in Fig. 4a) obtained upon either 595 nm or 561 nm excitation. The background also seems to exhibit a spectral blue shift as a function of temperature, with its maximum moving from 635 nm at room temperature to 620 nm at 4 K. Based on the temperature dependence of its spectral position, we attribute this background to intermediate gap states or defect states rather than excitons, trions or an indirect bandgap response (see ESI† Section 3).

Fig. 6d presents the temperature dependence of the average intensity ratio of the first two Raman peaks ( $E_{2g}/A_{1g}$ ). As shown in Fig. 4f, this ratio is not uniform over the pyramid, but is higher at the hollow pyramid middle than at the stair-like sides. This non-uniformity is most evident in the spectra obtained by 561 nm excitation (diamonds in Fig. 6d), as the  $A_{1g}$  peak in the spectra from the pyramid sides almost completely disappears at room temperature (see ESI Fig. S5†). For a 595 nm excitation, at room temperature the first Raman peak ( $E_{2g}$ ,  $2LA(M)$ ) is  $1.5\times$  higher than the second Raman peak ( $A_{1g}$ ) and at 4 K this ratio is exactly inverted (circles in Fig. 6d). The peak ratio upon 561 nm excitation of spectra taken at the pyramid middle follow a similar temperature-dependent behaviour (stars in Fig. 6d).

The temperature-dependent intensity increase of TMDs Raman peaks has been reported previously for horizontal TMDs layers, and is attributed to an increase in phonon thermal population.<sup>31,32,35</sup> The difference in intensity ratio between the  $E_{2g}$  and  $A_{1g}$  for the different excitation frequencies can be explained by the more resonant 595 nm laser exciting the Raman peaks differently than the out-of-resonance 561 nm laser.<sup>37,38</sup> The strength of the exciton–phonon interaction, and therefore the resonance condition, is different for the in-plane  $E_{2g}$  than the out-of-plane  $A_{1g}$  Raman modes.<sup>38,52</sup> This explains why the ratio  $E_{2g}/A_{1g}$  is higher for a 561 nm excitation, *e.g.*, out-of-resonance with the excitonic transition, than for the resonant 595 nm excitation. The Raman intensity ratio also depends on the layer thickness of the material.<sup>27</sup> However, the main difference in intensity ratio is reported between a monolayer and a bilayer, whereas we observe different relative Raman intensities between the few-layer pyramid crater and the thick pyramid edge. Moreover, the temperature-dependent behaviour of the Raman intensity also depends on the defect density in the sample.<sup>34</sup> These factors are not mutually independent, *e.g.*, the  $\text{WS}_2$  thickness influences the exciton–phonon interaction, the resonance of the excitation affects the influence of phonons and defects on the Raman intensity. The temperature dependence of the Raman peak intensities, excited with two different frequencies, is therefore an interplay between the phonon thermal population, the resonance conditions for the different phonon peaks and the defect density in the structure.

It is interesting to note in this context the intensity ratio of the first two Raman peaks on a  $\text{WS}_2$  monolayer, excited at 561 nm. This ratio is 1.4 at room temperature, much lower than both the intensity ratio at the hollow pyramid middle and at the stair-like sides, excited at 561 nm (see ESI Fig. S5†). Unexpectedly, this indicates a clear difference in structure and/or thickness between the  $\text{WS}_2$  monolayer and hollow pyramid. The large difference in intensity ratio on the hollow pyramid middle and the stair-like sides suggests a difference in atomic arrangement, pointing out that nanogeometrical differences induce spectral modifications.

### III. Conclusions

We have studied the optical response of hollow  $\text{WS}_2$  pyramids, comparing them with  $\text{WS}_2$  monolayers grown on the same substrate. The optical response of these nanostructures is completely different, as hollow  $\text{WS}_2$  exhibit a strongly reduced photoluminescence with respect to  $\text{WS}_2$  monolayers. This enables us to study the rich variety of Raman peaks that the pyramids exhibit as a result of the resonant excitation. Following the hypothesis of a multiphonon excitation involving the longitudinal acoustic phonon  $LA(M)$ , we are able to explain the origin of all 10–12 observed Raman resonances. In contrast with monolayers, the measured optical response of the pyramids is non-uniform in both intensity, intensity ratio between peaks, spectral shape and spectral position. We attribute the spectral differences between the hollow pyramid middle and the stair-like sides to differences in both nanogeometry and atomic arrangement. ADF-STEM measurements confirm variations in the atomic arrangement, where the level of disorder is more marked in the pyramid crater than on the sides. Next to a positional dependence, we measure the temperature dependent behaviour of the spectral response of the hollow  $\text{WS}_2$  pyramids. With decreasing temperature, the spectra change in intensity and shape. We see clear differences between spectra obtained with a resonant and out-of-resonance excitation laser. As the optical response of  $\text{WS}_2$  monolayers, exhibiting photoluminescence, is completely different, we therefore deduce to have fabricated a platform of structures with tunable optical properties. Both nanostructures offer exciting possibilities, with applications ranging from opto-electronics to non-linear optics.

### IV. Experimental section

The  $\text{WS}_2$  hollow pyramids are directly grown on a microchip using chemical vapour deposition (CVD) techniques. This microchip is composed of a silicon frame with nine windows over which a continuous silicon nitride ( $\text{Si}_3\text{N}_4$ ) film is spanned. Preceding the CVD growth procedure,<sup>16</sup> tungsten trioxide ( $\text{WO}_3$ ) is deposited onto the microchip. This deposition is achieved by dispersing 50 mg of  $\text{WO}_3$  in 1 mL of isopropanol, followed by a deposition by means of a pipette. The subsequent sulfurization process<sup>16</sup> is carried out in a gradient tube furnace from Carbolite Gero. The microchip is placed in the middle zone and a crucible holding 400 mg of sulfur is placed upstream from it. The middle zone is heated to 750 °C, and kept at this reaction





temperature for 1 hour after which the system is naturally cooled down to room temperature. Sulfurization is carried out under an argon flow of 150 sccm. The zone containing the sulfur is heated to 220 °C.

The optical measurements are performed using a home-built spectroscopy set-up. We placed the sample in a Montana cryostation S100, using Attocube ANPxy101/RES piezo scanners to perform the presented raster scans. The small cross-coupling between the in-plane and out-of-plane piezo scanners causes a skewing between the  $x$  and  $y$  axis of the spectral-feature maps depicted in this work. Comparing the maps with the optical and SEM images of the pyramids, we can correlate the position of certain spectral features with the position on the pyramid. The cryostation is cooled down from room temperature to 200 K, 100 K and 4 K. The sample is illuminated through an 0.85 NA Zeiss 100 $\times$  objective. Two continuous wave lasers are used, one with a wavelength of 595 nm and a power of 1.6 mW mm<sup>-2</sup>, and one with a wavelength of 561 nm and a power of 3.6 mW mm<sup>-2</sup>. To avoid the consequences of tight focussing on (circular) polarization, a 2 mm laser diameter is used, slightly underfilling the objective in the excitation path. This results in an excitation spot size of approximately 450 nm. A linear (vertical) polarization is used for the laser light. The sample emission is collected in reflection through the same objective as in excitation, and projected onto a CCD camera (Princeton Instruments ProEM 1024BX3) and spectrometer (Princeton Instruments SP2358) via a 4f lens system. The excitation light is filtered out using colour filters.

The transmission electron microscopy (TEM) measurements were carried out using an ARM200F Mono-JEOL microscope with Cs probed corrected. The microscope was operated at 200 kV both in TEM and STEM modes, with the monochromator on and a slit of 2  $\mu$ m inserted. For the atomic resolution ADF-STEM measurements, an objective aperture of 30  $\mu$ m and a camera length of 12 cm were used. The convergence semi-angle was 23 mrad.

## Conflicts of interest

The authors declare no competing interests.

## Acknowledgements

The authors acknowledge funding from ERC Starting Grant "TESLA" No. 805021. The authors acknowledge dr Martin Caldarola and dr Filippo Alpeggiani for their help in the data analysis.

## References

- 1 K. F. Mak, C. Lee, J. Hone, J. Shan and T. F. Heinz, Atomically thin mos2: a new direct-gap semiconductor, *Phys. Rev. Lett.*, 2010, **105**(13), 136805.
- 2 T. Cao, G. Wang, W. Han, H. Ye, C. Zhu, J. Shi, Q. Niu, P. Tan, E. Wang, B. Liu and J. Feng, Valley-selective circular dichroism of monolayer molybdenum disulfide, *Nat. Commun.*, 2012, **3**, 887.
- 3 X. Xu, Y. Wang, D. Xiao and T. F. Heinz, Spin and pseudospins in layered transition metal dichalcogenides, *Nat. Phys.*, 2014, **10**, 343.
- 4 B. Zhu, H. Zeng, J. Dai, Z. Gong and X. Cui, Anomalously robust valley polarization and valley coherence in bilayer ws2, *Proc. Natl. Acad. Sci. U. S. A.*, 2014, **111**(32), 11606–11611.
- 5 Y. J. Zhang, T. Oka, R. Suzuki, J. T. Ye and Y. Iwasa, Electrically switchable chiral light-emitting transistor, *Science*, 2014, **344**(6185), 725–728.
- 6 Q. H. Wang, K. Kalantar-Zadeh, A. Kis, J. N. Coleman and M. S. Strano, Electronics and optoelectronics of two-dimensional transition metal dichalcogenides, *Nat. Nanotechnol.*, 2012, **7**, 699.
- 7 K. F. Mak, K. L. McGill, J. Park and P. L. McEuen, The valley hall effect in mos2 transistors, *Science*, 2014, **344**(6191), 1489–1492.
- 8 J. R. Schaibley, H. Yu, G. Clark, P. Rivera, J. S. Ross, K. L. Seyler, Y. Wang and X. Xu, Valleytronics in 2d materials, *Nat. Rev. Mater.*, 2016, **1**, 16055.
- 9 S.-H. Gong, I. Komen, F. Alpeggiani and L. Kuipers, Nanoscale optical addressing of valley pseudospins through transverse optical spin, *Nano Lett.*, 2020, **20**(6), 4410–4415. PMID: 32406694.
- 10 J.-G. Song, J. Park, W. Lee, T. Choi, H. Jung, C. W. Lee, S.-H. Hwang, J. M. Myoung, J.-H. Jung, S.-H. Kim, C. Lansalot-Matras and H. Kim, Layer-controlled, wafer-scale, and conformal synthesis of tungsten disulfide nanosheets using atomic layer deposition, *ACS Nano*, 2013, **7**(12), 11333–11340.
- 11 Y. Zhang, Y. Zhang, Q. Ji, J. Ju, H. Yuan, J. Shi, T. Gao, D. Ma, M. Liu, Y. Chen, X. Song, H. Y. Hwang, Y. Cui and Z. Liu, Controlled growth of high-quality monolayer ws2 layers on sapphire and imaging its grain boundary, *ACS Nano*, 2013, **7**(10), 8963–8971.
- 12 C. Cong, J. Shang, X. Wu, B. Cao, N. Peimyoo, C. Qiu, L. Sun and Y. Ting, Synthesis and optical properties of large-area single-crystalline 2d semiconductor ws2 monolayer from chemical vapor deposition, *Adv. Opt. Mater.*, 2014, **2**(2), 131–136.
- 13 C. M. Orofeo, S. Suzuki, Y. Sekine and H. Hibino, Scalable synthesis of layer-controlled ws2 and mos2 sheets by sulfurization of thin metal films, *Appl. Phys. Lett.*, 2014, **105**(8), 083112.
- 14 A. Thangaraja, S. M. Shinde, G. Kalita and M. Tanemura, Effect of wo3 precursor and sulfurization process on ws2 crystals growth by atmospheric pressure cvd, *Mater. Lett.*, 2015, **156**, 156–160.
- 15 P. Liu, T. Luo, J. Xing, H. Xu, H. Hao, H. Liu and J. Dong, Large-area ws2 film with big single domains grown by chemical vapor deposition, *Nanoscale Res. Lett.*, 2017, **12**(1), 558.
- 16 S. E. van Heijst, M. Mukai, E. Okunishi, H. Hashiguchi, L. I. Roest, L. Maduro, J. Rojo and S. Conesa-Boj, Illuminating the electronic properties of ws2 polytypism with electron microscopy, *Ann. Phys.*, 2021, 2000499.



- 17 L. Zhang, K. Liu, A. B. Wong, J. Kim, X. Hong, C. Liu, T. Cao, S. G. Louie, F. Wang and P. Yang, Three-dimensional spirals of atomic layered mos<sub>2</sub>, *Nano Lett.*, 2014, **14**(11), 6418–6423.
- 18 P. V. Sarma, P. D. Patil, P. K. Barman, R. N. Kini and M. M. Shaijumon, Controllable growth of few-layer spiral ws<sub>2</sub>, *RSC Adv.*, 2016, **6**(1), 376–382.
- 19 A. V. Agrawal, R. Kumar, G. Yang, J. Bao, M. Kumar and M. Kumar, Enhanced adsorption sites in monolayer mos<sub>2</sub> pyramid structures for highly sensitive and fast hydrogen sensor, *Int. J. Hydrogen Energy*, 2020, **45**(15), 9268–9277.
- 20 P. Cheng, Q. Zhou, X. Hu, S. Su, X. Wang, M. Jin, L. Shui, X. Gao, Y. Guan, R. Nözel, G. Zhou, Z. Zhang and J. Liu, Transparent glass with the growth of pyramid-type mos<sub>2</sub> for highly efficient water disinfection under visible-light irradiation, *ACS Appl. Mater. Interfaces*, 2018, **10**(28), 23444–23450.
- 21 Q. Zhou, S. Su, P. Cheng, X. Hu, M. Zeng, X. Gao, Z. Zhang and J.-M. Liu, Robust ferromagnetism in zigzag-edge rich mos<sub>2</sub> pyramids, *Nanoscale*, 2018, **10**(24), 11578–11584.
- 22 J. Zheng, X. Yan, Z. Lu, H. Qiu, G. Xu, X. Zhou, P. Wang, X. Pan, K. Liu and L. Jiao, High-mobility multilayered mos<sub>2</sub> flakes with low contact resistance grown by chemical vapor deposition, *Adv. Mater.*, 2017, **29**(13), 1604540.
- 23 L. Chen, B. Liu, A. N. Abbas, Y. Ma, X. Fang, Y. Liu and C. Zhou, Screw-dislocation-driven growth of two-dimensional few-layer and pyramid-like wse<sub>2</sub> by sulfur-assisted chemical vapor deposition, *ACS Nano*, 2014, **8**(11), 11543–11551.
- 24 X. Fan, Y. Jiang, X. Zhuang, H. Liu, T. Xu, W. Zheng, P. Fan, H. Li, X. Wu, X. Zhu, Q. Zhang, H. Zhou, W. Hu, X. Wang, L. Sun, X. Duan and A. Pan, Broken symmetry induced strong nonlinear optical effects in spiral ws<sub>2</sub> nanosheets, *ACS Nano*, 2017, **11**(5), 4892–4898.
- 25 X. Lin, Y. Liu, K. Wang, W. Cong, W. Zhang, Y. Yan, Y. J. Li, J. Yao and Y. S. Zhao, Two-dimensional pyramid-like ws<sub>2</sub> layered structures for highly efficient edge second-harmonic generation, *ACS Nano*, 2018, **12**(1), 689–696.
- 26 C. Lee, H. Yan, L. E. Brus, T. F. Heinz, J. Hone and S. Ryu, Anomalous lattice vibrations of single- and few-layer mos<sub>2</sub>, *ACS Nano*, 2010, **4**(5), 2695–2700.
- 27 W. Zhao, Z. Ghorannevis, K. Kumar Amara, J. R. Pang, M. Toh, X. Zhang, C. Kloc, P. H. Tan and G. Eda, Lattice dynamics in mono- and few-layer sheets of ws<sub>2</sub> and wse<sub>2</sub>, *Nanoscale*, 2013, **5**, 9677–9683.
- 28 A. Berkdemir, H. R. Gutiérrez, A. R. Botello-Méndez, N. Perea-López, A. L. Elías, C.-I. Chia, B. Wang, V. H. Crespi, F. López-Urías, J.-C. Charlier, H. Terrones and M. Terrones, Identification of individual and few layers of ws<sub>2</sub> using Raman spectroscopy, *Sci. Rep.*, 2013, **3**(1), 1755.
- 29 A. A. Mitioglu, P. Plochocka, G. Deligeorgis, S. Anghel, L. Kulyuk and D. K. Maude, Second-order resonant Raman scattering in single-layer tungsten disulfide ws<sub>2</sub>, *Phys. Rev. B: Condens. Matter Mater. Phys.*, 2014, **89**(24), 245442.
- 30 M. R. Molas, K. Nogajewski, M. Potemski and B. Adam, Raman scattering excitation spectroscopy of monolayer ws<sub>2</sub>, *Sci. Rep.*, 2017, **7**(28698679), 5036.
- 31 N. Peimyoo, J. Shang, W. Yang, Y. Wang, C. Cong and Y. Ting, Thermal conductivity determination of suspended mono- and bilayer ws<sub>2</sub> by Raman spectroscopy, *Nano Res.*, 2015, **8**(4), 1210–1221.
- 32 A. P. S. Gaur, S. Sahoo, J. F. Scott and R. S. Katiyar, Electron-phonon interaction and double-resonance Raman studies in monolayer ws<sub>2</sub>, *J. Phys. Chem. C*, 2015, **119**(9), 5146–5151.
- 33 L. Xue, J. Li, K. Wang, X. Wang, S. Wang, X. Chu, M. Xu, X. Fang, Z. Wei, Y. Zhai and B. Zou, Pressure and temperature-dependent Raman spectra of mos<sub>2</sub> film, *Appl. Phys. Lett.*, 2016, **109**(24), 242101.
- 34 J. Li, W. Su, F. Chen, L. Fu, S. Ding, K. Song, X. Huang and L. Zhang, Atypical defect-mediated photoluminescence and resonance Raman spectroscopy of monolayer ws<sub>2</sub>, *J. Phys. Chem. C*, 2019, **123**(6), 3900–3907.
- 35 J.-He Fan, P. Gao, A.-M. Zhang, B.-R. Zhu, H.-L. Zeng, X.-D. Cui, R. He and Q.-M. Zhang, Resonance Raman scattering in bulk 2h-mx<sub>2</sub> (m=mo,w, x=s,se) and monolayer mos<sub>2</sub>, *J. Appl. Phys.*, 2014, **115**(5), 053527.
- 36 S.-Y. Chen, C. Zheng, M. S. Fuhrer and J. Yan., Helicity-resolved Raman scattering of mos<sub>2</sub>, mose<sub>2</sub>, ws<sub>2</sub>, and wse<sub>2</sub> atomic layers, *Nano Lett.*, 2015, **15**(4), 2526–2532.
- 37 B. R. Carvalho, L. M. Malard, J. M. Alves, C. Fantini and M. A. Pimenta, Symmetry-dependent exciton-phonon coupling in 2d and bulk mos<sub>2</sub> observed by resonance Raman scattering, *Phys. Rev. Lett.*, 2015, **114**, 136403.
- 38 E. del Corro, A. Botello-Méndez, Y. Gillet, A. L. Elias, H. Terrones, S. Feng, C. Fantini, D. Rhodes, N. Pradhan, L. Balicas, X. Gonze, J.-C. Charlier, M. Terrones and M. A. Pimenta, Atypical exciton-phonon interactions in ws<sub>2</sub> and wse<sub>2</sub> monolayers revealed by resonance Raman spectroscopy, *Nano Lett.*, 2016, **16**(4), 2363–2368. PMID: 26998817.
- 39 L. P. McDonnell, C.-C. Huang, Q. Cui, D. W. Hewak and D. C. Smith, Probing excitons, trions, and dark excitons in monolayer ws<sub>2</sub> using resonance Raman spectroscopy, *Nano Lett.*, 2018, **18**(2), 1428–1434.
- 40 J. E. Zucker, A. Pinczuk, D. S. Chemla, A. Gossard and W. Wiegmann, Raman scattering resonant with quasi-two-dimensional excitons in semiconductor quantum wells, *Phys. Rev. Lett.*, 1983, **51**, 1293–1296.
- 41 K. Gołasa, M. Grzeszczyk, P. Leszczyński, C. Faugeras, A. A. L. Nicolet, A. Wyszomolek, M. Potemski and A. Babiński, Multiphonon resonant Raman scattering in mos<sub>2</sub>, *Appl. Phys. Lett.*, 2014, **104**(9), 092106.
- 42 R. Yang, S. Feng, X. Lei, X. Mao, A. Nie, B. Wang, K. Luo, J. Xiang, F. Wen, C. Mu, Z. Zhao, B. Xu, H. Zeng, Y. Tian and Z. Liu, Effect of layer and stacking sequence in simultaneously grown 2h and 3r ws<sub>2</sub> atomic layers, *Nanotechnology*, 2019, **30**(34), 345203.
- 43 L. Du, Q. Zhang, T. Zhang, Z. Jia, J. Liang, G.-B. Liu, R. Yang, D. Shi, J. Xiang, K. Liu, Z. Sun, Y. Yao, Q. Zhang and G. Zhang, Robust circular polarization of indirect q-k transitions in bilayer 3r - Ws<sub>2</sub>, *Phys. Rev. B*, 2019, **100**, 161404.
- 44 M. Thirupuranthaka, R. V. Kashid, C. S. Rout and D. J. Late, Temperature dependent Raman spectroscopy of chemically



- derived few layer mos<sub>2</sub> and ws<sub>2</sub> nanosheets, *Appl. Phys. Lett.*, 2014, **104**(8), 081911.
- 45 J. H. Parker, D. W. Feldman and M. Ashkin, Raman scattering by silicon and germanium, *Phys. Rev.*, 1967, **155**(3), 712–714.
- 46 K. Uchinokura, T. Sekine and E. Matsuura, Raman scattering by silicon, *Solid State Commun.*, 1972, **11**(1), 47–49.
- 47 B. A. Weinstein and M. Cardona, Two-phonon Raman spectra of si and gap, *Solid State Commun.*, 1972, **10**(10), 961–965.
- 48 S. Mignuzzi, A. J. Pollard, N. Bonini, B. Brennan, I. S. Gilmore, M. A. Pimenta, D. Richards and D. Roy, Effect of disorder on Raman scattering of single-layer Mos<sub>2</sub>, *Phys. Rev. B: Condens. Matter Mater. Phys.*, 2015, **91**(19), 195411.
- 49 W. M. Parkin, A. Balan, L. Liang, P. M. Das, M. Lamparski, C. H. Naylor, J. A. Rodríguez-Manzo, A. T. Charlie Johnson, V. Meunier and M. Drndić, Raman shifts in electron-irradiated monolayer mos<sub>2</sub>, *ACS Nano*, 2016, **10**(4), 4134–4142.
- 50 C. Rice, R. J. Young, R. Zan, U. Bangert, D. Wolverson, T. Georgiou, R. Jalil and K. S. Novoselov, Raman-scattering measurements and first-principles calculations of strain-induced phonon shifts in monolayer mos<sub>2</sub>, *Phys. Rev. B: Condens. Matter Mater. Phys.*, 2013, **87**(8), 081307.
- 51 L. Yang, X. Cui, J. Zhang, K. Wang, M. Shen, S. Zeng, S. A. Dayeh, F. Liang and B. Xiang, Lattice strain effects on the optical properties of mos<sub>2</sub> nanosheets, *Sci. Rep.*, 2014, **4**(1), 5649.
- 52 D. Mastrippolito, S. Palleschi, G. D'Olimpio, A. Politano, M. Nardone, P. Benassi and L. Ottaviano, Exciton-phonon coupling and power dependent room temperature photoluminescence of sulphur vacancy doped mos<sub>2</sub> via controlled thermal annealing, *Nanoscale*, 2020, **12**(36), 18899–18907.

